Differential requirements for mitochondrial electron transport chain components in the adult murine liver.

Nicholas P. Lesner[1], Xun Wang[1], Anderson Frank[2], Sara House[1], Spencer D. Shelton[1], David G. McFadden[2], Ralph J. DeBerardinis[1,3,4], Prashant Mishra[1,3,5]

[1]Children's Medical Center Research Institute, University of Texas Southwestern Medical Center, Dallas, TX 75390.

[2]Department of Biochemistry, University of Texas Southwestern Medical Center, Dallas, TX 75390.

[3]Department of Pediatrics, University of Texas Southwestern Medical Center, Dallas, TX 75390.

[4]Howard Hughes Medical Institute, University of Texas Southwestern Medical Center, Dallas, TX 75390.

[5]Green Center for Systems Biology, University of Texas Southwestern Medical Center, Dallas, TX 75390.

*Correspondence to: prashant.mishra@utsouthwestern.edu

Summary

Mitochondrial electron transport chain (ETC) dysfunction is a common cause of metabolic disease in humans, but the mechanisms underlying tissue specific phenotypes are not understood. Complex I (cI) is classically considered the entry point for electrons into the ETC, and *in vitro* experiments indicate that cI is required for maintenance of the NAD^+/NADH ratio, an indicator of cellular redox status. This finding has largely not been tested *in vivo.* Here, we report that mitochondrial complex I (cI) is dispensable for homeostasis of the adult mouse liver; animals with hepatocyte-specific loss of cI function display no overt phenotypes or signs of liver damage, and maintain liver function and redox status. Further analysis of cI-deficient livers did not reveal significant proteomic or metabolic changes, indicating little to no compensation is required in the setting of complex I loss. In contrast, complex IV (cIV) dysfunction in adult hepatocytes results in decreased liver function, steatosis, and liver damage, accompanied by significant metabolomic and proteomic perturbations. Correspondingly, we find that complex I-deficient livers are reliant on an alternative pathway, whereby electrons are donated to the ETC via dihydroorotate dehydrogenase, to maintain redox status. Our results support a model whereby complex I loss is tolerated in the mouse liver because hepatocytes make use of alternative electron donors to fuel the mitochondrial ETC.

52 **Introduction**

53 Mitochondrial ETC disease in humans exhibits a striking tissue specificity, whereby
54 mutations in distinct ETC components are causative for specific and non-overlapping
55 syndromes (*1*). As an example, genetic dysfunction of mitochondrial complex I (cI) is
56 associated with neurological disease including Leigh syndrome (characterized by severe
57 loss of motor abilities, necrotizing brain lesions and early death), and Leber Hereditary
58 Optic Neuropathy (characterized by bilateral loss of vision in early adulthood due to
59 degeneration of the optic nerve) (*2-4*). The mechanisms underlying sensitivity of the
60 nervous system, with sparing of other organ systems, in the setting of complex I loss is
61 not understood. In contrast, mutations in other mitochondrial ETC components have been
62 associated with multi-organ diseases, and the basis for tissue specificity in those diseases
63 is also unclear (*5*).

64 Liver involvement is a common component of mitochondrial diseases, present in
65 approximately 20% of patients (*6, 7*), as well as being associated with specific syndromes
66 caused by mutations in distinct ETC-related components (*8-12*). Common findings in
67 affected patients include hepatomegaly, steatosis, cholestasis and additional metabolic
68 abnormalities associated with liver failure (*12-15*). Genetic analysis of patients has
69 revealed mutations in genes which influence multiple components of the ETC (e.g.,
70 *POLG*, *LARS*, *DGUOK*) (*10*). With respect to single-complex diseases, mutations in
71 *SCO1*, an assembly protein for mitochondrial complex IV (cIV), and mutations in *BCS1L*,
72 a chaperone protein for mitochondrial complex III, have been associated with liver failure
73 (*8, 16, 17*). Interestingly, single-complex diseases associated with other components of

74 the ETC (complex I and complex II) do not typically present with liver failure, despite their
75 placement directly upstream of cIV.

76 The ETC functions to transfer electrons (from the oxidation of nutrients) to O_2, as
77 a final electron acceptor; this process is coupled to the formation of an electrochemical
78 gradient across the mitochondrial inner membrane and the production of ATP.
79 Mitochondrial complex I is the largest protein complex of the ETC, and is commonly
80 considered the primary entry point for electrons into the ETC: In cultured cells, cI is
81 required for maintenance of cellular redox status (assessed by the NAD^+/NADH ratio) via
82 its role in NADH oxidation, and subsequent electron transfer to ubiquinone (CoQ) (*18*).
83 Complex I is composed of 14 core subunits, plus an additional 31 accessory subunits
84 (*19*). Published mouse models of complex I deficiency have largely focused on accessory
85 subunits, including deletion of *Ndufs4*, *Ndufs6*, and *Ndufa5*, which result in neurological
86 and cardiac phenotypes associated with partial loss of complex I function (*20-22*); no liver
87 phenotypes or metabolic perturbations were reported in these mice (*23*). A recent report
88 conditionally deleted *Ndufs3*, a core subunit of cI, in skeletal muscle, resulting in
89 progressive myopathy associated with significant reduction of cI activity (*24*). Thus, to
90 date, mouse models have supported an essential role for cI *in vivo* in the central nervous
91 system and muscle. Here, we report that deletion of the core subunit, *Ndufa9*, results in
92 complete loss of cI function, but is well-tolerated in the adult mouse liver. Further analysis
93 reveals intact liver function in *ndufa9*$^{-/-}$ animals, which is not accompanied by significant
94 metabolic alterations or changes in redox status. This is in contrast with hepatocyte-
95 specific deletion of the complex IV component *cox10,* which results in altered redox status
96 and impaired liver function. These results support a model in which cI is not an essential

upstream component of the ETC in adult mammalian liver, in contrast to the conventional view of cI function.

121 **RESULTS**

122 **Mitochondrial complex I function is dispensable for homeostatic function of adult**
123 **murine hepatocytes**

124 To understand how liver cells respond to loss of complex I, we made use of a conditional
125 allele of the core subunit *Ndufa9*. *Ndufa9* deletion in mouse fibroblasts results in loss of
126 mitochondrial respiratory function, as well as a significant drop in the NAD^+/NADH ratio
127 (Figure 1 – figure supplement 1A,B), indicating that Ndufa9 is critical for redox status in
128 these cultured cells. We depleted Ndufa9 in livers of adult mice, making use of adeno-
129 associated virus 8 (AAV8)-mediated Cre recombination driven by the liver specific TBG
130 promoter in *ndufa9*$^{flox/flox}$ animals (see Methods). *ndufa9*$^{flox/flox}$ adult animals were injected
131 with control AAV8-GFP virus (hereafter "*ndufa9*$^{f/f}$") or AAV8-Cre virus (hereafter "*ndufa9*$^{-}$
132 $^{/-}$"). At 4 weeks post-AAV administration, AAV-Cre injected animals exhibited loss of
133 Ndufa9 mRNA and protein in hepatocytes, as well as loss of mitochondrial oxygen
134 consumption (Figure 1A-C). At this time point, *ndufa9*$^{-/-}$ livers displayed no differences in
135 gross physiology (Figure 1D) or liver/body weight ratio (Figure 1F). Histological analysis
136 of liver sections revealed no significant pathology, including no evidence of steatosis (Oil
137 Red O staining) or glycogen loss (PAS staining) (Figure 1E). Liver function was
138 maintained in *ndufa9*$^{-/-}$ livers as indicated by unaltered levels of fasting glucose (Figure
139 1G) and circulating indicators of liver function and damage (Figure 1H,I). Similar results
140 were observed in mice at eight weeks post-AAV injection (Figure 1 – figure supplement
141 1C-G). Thus, complex I loss is well-tolerated in adult mouse hepatocytes under
142 homeostatic conditions, with no discernable effects on tissue function, or evidence of
143 tissue damage.

144 Complex I inhibition is often associated with elevated reactive oxygen species (*25,*
145 *26*). In *ndufa9*$^{-/-}$ livers, we observed a small decrease in the reduced to oxidized
146 glutathione (GSH / GSSG) ratio, indicating increased oxidative stress in the setting of
147 complex I deficiency (Figure 2A). Surprisingly, we did not observe altered NAD^+/NADH or
148 NADPH/$NADP^+$ ratios in *ndufa9*$^{-/-}$ liver (Figure 2B). We additionally examined
149 compartment specific redox status by calculating pyruvate / lactate and acetoacetate / β-
150 hydroxybutyrate ratios, which are indicative of cytosolic and mitochondrial redox status
151 respectively; neither compartment display evidence of altered redox status (Figure 2C).
152 A recent report suggests that circulating α-hydroxybutyrate levels serves as a marker of
153 hepatic redox stress (*27*). *ndufa9*$^{-/-}$ animals did not display alterations in tissue or plasma
154 α-hydroxybutyrate levels (Figure 2D). Thus, complex I function is not required for
155 maintenance of hepatic redox status, in contrast to its established role in cultured cells
156 (Figure 1 – figure supplement 1A,B) (*18*).

157 To examine potential compensatory mechanisms that may be enabled in the
158 setting of complex I inhibition, we assessed changes in the proteome and metabolome,
159 comparing *ndufa9*$^{f/f}$ and *ndufa9*$^{-/-}$ whole livers. Our proteomics analysis detected 3353
160 proteins with high confidence; however, only 6 proteins were significantly upregulated
161 ($\log_2$(fold change) > 1, Adjusted p-val < 0.05), and 20 proteins were significantly
162 downregulated ($\log_2$(Fold Change) < -1; Adjusted p-val < 0.05) (Figure 2 – figure
163 supplement 1). Of the down-regulated proteins, the majority were components of complex
164 I (Figure 2E), consistent with destabilization of cI in the setting of Ndufa9 subunit loss. In
165 addition, we did not detect significant changes in total mitochondrial content in *ndufa9*$^{-/-}$
166 livers, as indicated by measurement of mitochondrial genome and protein content (Figure

167 2F,G). We assessed metabolism in livers of fasted mice, using LC/Q-TOF mass
168 spectrometry based metabolomics. Steady-state targeted metabolomic analysis of >150
169 metabolites revealed only a single statistical metabolite difference (Figure 2H, Figure 2 –
170 figure supplement 1), and no significant changes in mitochondrial TCA cycle metabolites
171 (Figure 2I). Together, these results indicate that complex I is largely dispensable for
172 homeostatic function in the adult mouse liver, without significant metabolic or proteomic
173 compensation.
174
175 **Mitochondrial complex IV is required in adult hepatocytes.**
176 To further explore a role for the mitochondrial ETC, we examined the requirement for
177 complex IV, making use of a *cox10*^{flox} allele (*28*). Cox10 is a required assembly
178 component of complex IV, and Cox10 deletion in skeletal muscle is associated with
179 diminished cIV activity accompanied by myopathy (*28*). A previous report utilizing this
180 allele in combination with the liver-specific Albumin-Cre transgenic reporter revealed
181 partially penetrant phenotypes dependent on the transgene dosage (*29*), suggesting that
182 the mitochondrial ETC is required for liver homeostasis. Thus, we made use of AAV-
183 delivery of Cre recombinase to *cox10*$^{f/f}$ animals to investigate its role in the adult liver.
184 Similar to above, we injected *cox10*$^{f/f}$ animals with AAV-GFP or AAV-Cre and
185 characterized liver physiology at 4 and 8 weeks post-injection. At 4 weeks post-injection,
186 AAV-Cre injected animals demonstrated significant reductions in Cox10 mRNA and
187 protein (Figure 3A,B) and complex IV activity (Figure 3C). By 8 weeks post-AAV
188 administration, *cox10*$^{-/-}$ livers were grossly enlarged and pale in color, as compared with
189 wild-type livers (Figure 3D,F). Histological analysis of liver sections revealed widespread

190 lipid accumulation indicating hepatic steatosis (Oil Red O staining), as well as decreased
191 glycogen accumulation (PAS staining) (Figure 3E). Correspondingly, fasting glucose
192 levels were decreased in animals with *cox10*$^{-/-}$ livers (Figure 3G). To directly probe
193 gluconeogenesis, fasted mice were challenged with a [U-^{13}C]-lactate/pyruvate tolerance
194 test; animals with *cox10*$^{-/-}$ livers were unresponsive as compared with wild-type animals
195 (Figure 3H,I, Figure 3 – figure supplement 1A). Additional plasma indicators of liver
196 function were diminished in *cox10*$^{-/-}$ animals, including decreased plasma total protein
197 and increased plasma bilirubin (Figure 3J). We also observed significant elevations in
198 ALT and AST, suggestive of liver damage (Figure 3K). Thus, in contrast to loss of complex
199 I, the loss of complex IV in adult hepatocytes is associated with hepatic steatosis,
200 diminished liver function and evidence of liver damage.

201 *cox10*$^{-/-}$ livers exhibited increased oxidative stress (lowering of the GSH / GSSG
202 ratio), consistent with mitochondrial ETC dysfunction (Figure 4A). In contrast to cI-
203 deficient livers, cIV deficiency significantly impacted the redox status of the cell, as
204 measured by the NAD^+ / NADH ratio (Figure 4B). We observed altered ratios of both
205 pyruvate / lactate and acetoacetate / β-hydroxybutyrate, indicating impaired redox status
206 in both the cytosol and mitochondrial compartments (Figure 4C). Interestingly,
207 assessment of tissue and plasma α-hydroxybutyrate levels, revealed decreases in the
208 setting of cIV loss. Thus, impairment of mitochondrial complex IV has both biochemical
209 and functional consequences in the adult liver, and is acutely required for maintenance
210 of cellular redox status.

211 To probe the effects of complex IV loss in mammalian liver, we assessed proteome
212 changes between *cox10*$^{f/f}$ and *cox10*$^{-/-}$ livers (Figure 4E, Figure 4 – figure supplement 2).

213 A large number of proteins were significantly up-regulated, and this group was enriched
214 for proteins that localize to mitochondria (Figure 4E). Consistent with this, we observed
215 significant increases in total mitochondrial content in *cox10*$^{-/-}$ livers, as measured by both
216 mitochondrial genome and protein content (Figure 4F,G). We identified a number of
217 complex IV components among the down-regulated proteins (Figure 4E), consistent with
218 destabilization of intact complex IV. In addition, gene-ontology analysis of down-regulated
219 proteins revealed enrichment of several metabolic pathways (Figure 4 – figure
220 supplement 1A, Figure 4 – figure supplement 2), indicating extensive metabolic
221 compensation in mutant livers.

222 Steady-state metabolomic analysis of *cox10*$^{f/f}$ and *cox10*$^{-/-}$ livers revealed
223 significant alterations in a subset of metabolites (Figure 4H, Figure 4 – figure supplement
224 2). Levels of mitochondrial TCA cycle metabolites were largely maintained, although we
225 observed a significant increase in 2-hydroxyglutarate levels, which has been previously
226 observed in the setting of mitochondrial dysfunction (Figure 4I) (*30*). We observed
227 significant upregulation in cholate species, consistent with cholestasis and hepatomegaly
228 in these animals (Figure 4H, Figure 4 – figure supplement 1C). Upregulated metabolites
229 were also highly enriched for long-chain acylcarnitine fatty acid species, consistent with
230 a fatty acid oxidation defect (Figure 4H, Figure 4 –figure supplement 1B). Concomitantly,
231 we observed a significant decrease in β-hydroxybutyrate levels, a byproduct of fatty-acid
232 oxidation (Figure 4J). Interestingly, downregulated metabolites were enriched for several
233 electron carriers, including pyruvate, ascorbate and tetrahydrobiopterin (Figure 4H,J),
234 suggesting that the mitochondrial ETC may be interacting with electron transfer from
235 multiple sources.

236

237 **DHODH activity maintains cellular redox status in the absence of mitochondrial**

238 **complex I.**

239 The phenotype of *cox10*$^{-/-}$ livers noted above indicates that the mitochondrial ETC is
240 required for liver homeostasis. However, the incongruence of phenotypes between cI and
241 cIV hepatic deficiency led us to consider alternative routes for electrons to enter the
242 mitochondrial ETC, including complex II and DHODH (Figure 5A). Dihydroorotate
243 dehydrogenase (DHODH) is highly expressed in the mammalian liver, localized to the
244 mitochondrial inner membrane, and transfers electrons from dihydroorotate to coenzyme
245 Q as part of the pyrimidine biosynthesis pathway (Figure 5A). Assessment of metabolites
246 in this pathway revealed that levels of a subset of these metabolites (including aspartate,
247 UDP-glucose and thymidine) were altered in the setting of cIV-deficiency (Figure 4K). In
248 contrast, we did not observe perturbations in succinate levels or TCA cycle metabolites
249 in *cox10*$^{-/-}$ livers (Figure 4I).

250 By donating electrons directly to coenzyme Q, DHODH activity offers a route to
251 bypass cI and maintain ETC activity (Figure 5A). In complex I deficient livers, DHODH
252 levels were not altered and metabolites in the pyrimidine synthesis pathway were not
253 perturbed (Figure 5B,C). We therefore treated *ndufa9*$^{f/f}$ and *ndufa9*$^{-/-}$ animals with
254 brequinar, a DHODH inhibitor. DHODH inhibition is associated with hepatotoxicity in
255 humans; however, we used a dosage which did not affect liver physiology (Figure 5 –
256 figure supplement 1A-D), based on a previous protocol (*31*). Brequinar treatment
257 increased dihydroorotate levels in both *ndufa9*$^{f/f}$ and *ndufa9*$^{-/-}$ livers, indicating that
258 DHODH activity was inhibited (Figure 5D). In vehicle-treated animals, NAD^+ / NADH ratios

259 were not significantly altered by cI loss. However, in the setting of DHODH inhibition,
260 complex I loss significantly lowered the NAD^+ / NADH ratio (Figure 5E). This effect was
261 not due to altered levels of pyrimidine pathway metabolites (Figure 5 – figure supplement
262 1E), suggesting a direct role for electron transfer into ETC by DHODH. These findings
263 indicate that although complex I is largely dispensable in the adult liver, it can interact
264 with alternative electron donor pathways to regulate cellular redox status.

265
266
267
268
269
270
271
272
273
274
275
276
277
278
279
280
281

282 **Discussion:**

283 The lack of a requirement for complex I in adult mammalian liver is not consistent with a
284 key role for complex I in electron entry to the ETC in this tissue; in particular, we observed
285 no alterations in mitochondrial of cytosol redox status in cI-deficient liver, or evidence of
286 significant metabolic compensation. The liver is known to have relatively low flux through
287 PDH, the major entry point of carbons to the TCA cycle which generates NADH for cI
288 function (*32, 33*); thus, our data is consistent with a model in which the hepatic TCA cycle
289 does not play a prominent role in nutrient oxidation via the generation of mitochondrial
290 NADH. The impact of cIV deficiency on cellular redox status indicates that the
291 mitochondrial ETC is critical for removing electrons via transfer to oxygen, and thus,
292 alternative electron donors are likely to fuel the ETC, including DHODH. We show that
293 combined inhibition of DHODH and complex I is sufficient to impact redox status;
294 however, there may still be additional important electron sources (such as complex II)
295 which play a prominent role in the liver. A limitation of our study is that we have examined
296 homeostatic functions of the mouse liver, and it is possible that complex I does have a
297 required role in the setting of hepatic stressors (e.g., high fat diet, regeneration), and it
298 will be important to assess these scenarios in future work.

299 Indeed, the relevant and high flux modes of electron entry into the ETC may be
300 different among distinct tissues, and this provides a plausible hypothesis for the non-
301 overlapping syndromes present in mitochondrial ETC diseases affecting different
302 components. As an upstream component of the ETC, cI mutations may manifest in a
303 narrow set of tissues systems which rely on mitochondrial NADH to fuel respiration. In
304 contrast, complex IV, the terminal component of the ETC which feeds electrons to oxygen

305 as a final electron acceptor, might be predicted to have effects in a wider variety of tissues,
306 particularly those which do not significantly generate and export lactate as a means to
307 remove electrons. Understanding the key ETC fuel sources in both normal and stressed
308 tissue systems will therefore provide insight into the pathophysiological processes which
309 occur downstream of specific mitochondrial mutations.
310
311
312 **Acknowledgments:**
313 We thank the Hao Zhu lab for assistance with hepatocyte isolation experiments, the UT
314 Southwestern Metabolic Phenotyping Core for plasma analysis, the UT Southwestern
315 Proteomics Core, the CRI Metabolomics Facility, the Biochemistry Metabolomics Core
316 and members of the Mishra and DeBerardinis laboratories for helpful discussions and
317 suggestions during this project. Diagrams were created with BioRender.com. **Funding:**
318 This work was supported by funding from the United Mitochondrial Disease Foundation
319 (Research Grant to P.M.), the National Institutes of Health (1DP2ES030449-01 from
320 NIEHS to P.M., 1R01AR073217-01 from NIAMS to P.M., 1F31-DK122676 from NIDDK
321 to N.P.L.), the Moody Medical Research Institute (Research Grant to P.M.), and the
322 National Science Foundation (GRFP 2019281210 award to S.D.S.). **Author
323 Contributions: N.P.L.:** Conceptualization, Methodology, Validation, Formal analysis,
324 Investigation, Data curation, Writing – Original Draft, Writing – Review & Editing,
325 Visualization. **X.W.:** Investigation. **S.H.:** Investigation. **A.F.:** Investigation. **S.D.S:**
326 Investigation. **D.G.M.:** Resources. **R.J.D.:** Resources, Writing – Review & Editing. **P.M.:**
327 Conceptualization, Methodology, Formal analysis, Resources, Data curation, Writing –

328 Original Draft, Writing – Review & Editing, Visualization, Supervision, Funding acquisition.

329 **Competing Interests:** R.J.D. is an advisor to Agios Pharmaceuticals. **Data and material**

330 **availability:** All data and materials are provided within the manuscript and supplementary

331 materials, or available upon reasonable request.

332

333 **References:**

334 1. G. S. Gorman, P. F. Chinnery, S. DiMauro, M. Hirano, Y. Koga, R. McFarland, A.
335 Suomalainen, D. R. Thorburn, M. Zeviani, D. M. Turnbull, Mitochondrial
336 diseases. *Nature reviews. Disease primers* **2**, 16080 (2016); published online
337 EpubOct 20 (10.1038/nrdp.2016.80).
338 2. R. J. Rodenburg, Mitochondrial complex I-linked disease. *Biochimica et*
339 *biophysica acta* **1857**, 938-945 (2016); published online EpubJul
340 (10.1016/j.bbabio.2016.02.012).
341 3. M. A. Martin, A. Blazquez, L. G. Gutierrez-Solana, D. Fernandez-Moreira, P.
342 Briones, A. L. Andreu, R. Garesse, Y. Campos, J. Arenas, Leigh syndrome
343 associated with mitochondrial complex I deficiency due to a novel mutation in the
344 NDUFS1 gene. *Archives of neurology* **62**, 659-661 (2005); published online
345 EpubApr (10.1001/archneur.62.4.659).
346 4. F. Distelmaier, W. J. Koopman, L. P. van den Heuvel, R. J. Rodenburg, E.
347 Mayatepek, P. H. Willems, J. A. Smeitink, Mitochondrial complex I deficiency:
348 from organelle dysfunction to clinical disease. *Brain : a journal of neurology* **132**,
349 833-842 (2009); published online EpubApr (10.1093/brain/awp058).
350 5. S. T. Ahmed, L. Craven, O. M. Russell, D. M. Turnbull, A. E. Vincent, Diagnosis
351 and Treatment of Mitochondrial Myopathies. *Neurotherapeutics : the journal of*
352 *the American Society for Experimental NeuroTherapeutics* **15**, 943-953 (2018);
353 published online EpubOct (10.1007/s13311-018-00674-4).
354 6. W. S. Lee, R. J. Sokol, Mitochondrial hepatopathies: advances in genetics and
355 pathogenesis. *Hepatology* **45**, 1555-1565 (2007); published online EpubJun
356 (10.1002/hep.21710).

357 7. S. Rahman, Gastrointestinal and hepatic manifestations of mitochondrial
358 disorders. *Journal of inherited metabolic disease* **36**, 659-673 (2013); published
359 online EpubJul (10.1007/s10545-013-9614-2).
360 8. I. Valnot, S. Osmond, N. Gigarel, B. Mehaye, J. Amiel, V. Cormier-Daire, A.
361 Munnich, J. P. Bonnefont, P. Rustin, A. Rotig, Mutations of the SCO1 gene in
362 mitochondrial cytochrome c oxidase deficiency with neonatal-onset hepatic
363 failure and encephalopathy. *American journal of human genetics* **67**, 1104-1109
364 (2000); published online EpubNov (10.1016/S0002-9297(07)62940-1).
365 9. J. P. Casey, P. McGettigan, N. Lynam-Lennon, M. McDermott, R. Regan, J.
366 Conroy, B. Bourke, J. O'Sullivan, E. Crushell, S. Lynch, S. Ennis, Identification of
367 a mutation in LARS as a novel cause of infantile hepatopathy. *Molecular genetics*
368 *and metabolism* **106**, 351-358 (2012); published online EpubJul
369 (10.1016/j.ymgme.2012.04.017).
370 10. W. S. Lee, R. J. Sokol, Liver disease in mitochondrial disorders. *Seminars in liver*
371 *disease* **27**, 259-273 (2007); published online EpubAug (10.1055/s-2007-
372 985071).
373 11. A. A. Morris, J. W. Taanman, J. Blake, J. M. Cooper, B. D. Lake, M. Malone, S.
374 Love, P. T. Clayton, J. V. Leonard, A. H. Schapira, Liver failure associated with
375 mitochondrial DNA depletion. *Journal of hepatology* **28**, 556-563 (1998);
376 published online EpubApr (10.1016/s0168-8278(98)80278-x).
377 12. H. Koh, G. S. Park, S. M. Shin, C. E. Park, S. Kim, S. J. Han, H. Q. Pham, J. H.
378 Shin, D. W. Lee, Mitochondrial Mutations in Cholestatic Liver Disease with Biliary
379 Atresia. *Scientific reports* **8**, 905 (2018); published online EpubJan 17
380 (10.1038/s41598-017-18958-8).
381 13. J. P. Molleston, R. J. Sokol, W. Karnsakul, A. Miethke, S. Horslen, J. C. Magee,
382 R. Romero, R. H. Squires, J. L. Van Hove, N. Childhood Liver Disease Research
383 Education, Evaluation of the child with suspected mitochondrial liver disease.
384 *Journal of pediatric gastroenterology and nutrition* **57**, 269-276 (2013); published
385 online EpubSep (10.1097/MPG.0b013e31829ef67a).
386 14. K. Cloots, J. Verbeek, H. Orlent, W. Meersseman, D. Cassiman, Mitochondrial
387 hepatopathy in adults: a case series and review of the literature. *European*

388 *journal of gastroenterology & hepatology* **25**, 892-898 (2013); published online
389 EpubAug (10.1097/MEG.0b013e32835ee629).
390 15. P. F. Chinnery, S. DiMauro, Mitochondrial hepatopathies. *Journal of hepatology*
391 **43**, 207-209 (2005); published online EpubAug (10.1016/j.jhep.2005.05.012).
392 16. L. De Meirleir, S. Seneca, E. Damis, B. Sepulchre, A. Hoorens, E. Gerlo, M. T.
393 Garcia Silva, E. M. Hernandez, W. Lissens, R. Van Coster, Clinical and
394 diagnostic characteristics of complex III deficiency due to mutations in the BCS1L
395 gene. *American journal of medical genetics. Part A* **121A**, 126-131 (2003);
396 published online EpubAug 30 (10.1002/ajmg.a.20171).
397 17. P. de Lonlay, I. Valnot, A. Barrientos, M. Gorbatyuk, A. Tzagoloff, J. W.
398 Taanman, E. Benayoun, D. Chretien, N. Kadhom, A. Lombes, H. O. de Baulny,
399 P. Niaudet, A. Munnich, P. Rustin, A. Rotig, A mutant mitochondrial respiratory
400 chain assembly protein causes complex III deficiency in patients with
401 tubulopathy, encephalopathy and liver failure. *Nature genetics* **29**, 57-60 (2001);
402 published online EpubSep (10.1038/ng706).
403 18. L. B. Sullivan, D. Y. Gui, A. M. Hosios, L. N. Bush, E. Freinkman, M. G. Vander
404 Heiden, Supporting Aspartate Biosynthesis Is an Essential Function of
405 Respiration in Proliferating Cells. *Cell* **162**, 552-563 (2015); published online
406 EpubJul 30 (10.1016/j.cell.2015.07.017).
407 19. L. K. Sharma, J. Lu, Y. Bai, Mitochondrial respiratory complex I: structure,
408 function and implication in human diseases. *Current medicinal chemistry* **16**,
409 1266-1277 (2009)10.2174/092986709787846578).
410 20. S. E. Kruse, W. C. Watt, D. J. Marcinek, R. P. Kapur, K. A. Schenkman, R. D.
411 Palmiter, Mice with mitochondrial complex I deficiency develop a fatal
412 encephalomyopathy. *Cell metabolism* **7**, 312-320 (2008); published online
413 EpubApr (10.1016/j.cmet.2008.02.004).
414 21. S. Peralta, A. Torraco, T. Wenz, S. Garcia, F. Diaz, C. T. Moraes, Partial
415 complex I deficiency due to the CNS conditional ablation of Ndufa5 results in a
416 mild chronic encephalopathy but no increase in oxidative damage. *Human*
417 *molecular genetics* **23**, 1399-1412 (2014); published online EpubMar 15
418 (10.1093/hmg/ddt526).

419 22. B. X. Ke, S. Pepe, D. R. Grubb, J. C. Komen, A. Laskowski, F. A. Rodda, B. M.
420 Hardman, J. J. Pitt, M. T. Ryan, M. Lazarou, J. Koleff, M. M. Cheung, J. J.
421 Smolich, D. R. Thorburn, Tissue-specific splicing of an Ndufs6 gene-trap
422 insertion generates a mitochondrial complex I deficiency-specific
423 cardiomyopathy. *Proceedings of the National Academy of Sciences of the United*
424 *States of America* **109**, 6165-6170 (2012); published online EpubApr 17
425 (10.1073/pnas.1113987109).
426 23. L. Yang, J. C. Garcia Canaveras, Z. Chen, L. Wang, L. Liang, C. Jang, J. A.
427 Mayr, Z. Zhang, J. M. Ghergurovich, L. Zhan, S. Joshi, Z. Hu, M. R. McReynolds,
428 X. Su, E. White, R. J. Morscher, J. D. Rabinowitz, Serine Catabolism Feeds
429 NADH when Respiration Is Impaired. *Cell metabolism* **31**, 809-821 e806 (2020);
430 published online EpubApr 7 (10.1016/j.cmet.2020.02.017).
431 24. C. V. Pereira, S. Peralta, T. Arguello, S. R. Bacman, F. Diaz, C. T. Moraes,
432 Myopathy reversion in mice after restauration of mitochondrial complex I. *EMBO*
433 *molecular medicine* **12**, e10674 (2020); published online EpubFeb 7
434 (10.15252/emmm.201910674).
435 25. N. Li, K. Ragheb, G. Lawler, J. Sturgis, B. Rajwa, J. A. Melendez, J. P. Robinson,
436 Mitochondrial complex I inhibitor rotenone induces apoptosis through enhancing
437 mitochondrial reactive oxygen species production. *The Journal of biological*
438 *chemistry* **278**, 8516-8525 (2003); published online EpubMar 7
439 (10.1074/jbc.M210432200).
440 26. R. Fato, C. Bergamini, M. Bortolus, A. L. Maniero, S. Leoni, T. Ohnishi, G. Lenaz,
441 Differential effects of mitochondrial Complex I inhibitors on production of reactive
442 oxygen species. *Biochimica et biophysica acta* **1787**, 384-392 (2009); published
443 online EpubMay (10.1016/j.bbabio.2008.11.003).
444 27. R. P. Goodman, A. L. Markhard, H. Shah, R. Sharma, O. S. Skinner, C. B. Clish,
445 A. Deik, A. Patgiri, Y. H. Hsu, R. Masia, H. L. Noh, S. Suk, O. Goldberger, J. N.
446 Hirschhorn, G. Yellen, J. K. Kim, V. K. Mootha, Hepatic NADH reductive stress
447 underlies common variation in metabolic traits. *Nature* **583**, 122-126 (2020);
448 published online EpubJul (10.1038/s41586-020-2337-2).

449 28. F. Diaz, C. K. Thomas, S. Garcia, D. Hernandez, C. T. Moraes, Mice lacking
450 COX10 in skeletal muscle recapitulate the phenotype of progressive
451 mitochondrial myopathies associated with cytochrome c oxidase deficiency.
452 *Human molecular genetics* **14**, 2737-2748 (2005); published online EpubSep 15
453 (10.1093/hmg/ddi307).
454 29. F. Diaz, S. Garcia, D. Hernandez, A. Regev, A. Rebelo, J. Oca-Cossio, C. T.
455 Moraes, Pathophysiology and fate of hepatocytes in a mouse model of
456 mitochondrial hepatopathies. *Gut* **57**, 232-242 (2008); published online EpubFeb
457 (10.1136/gut.2006.119180).
458 30. R. J. Hunt, L. Granat, G. S. McElroy, R. Ranganathan, N. S. Chandel, J. M.
459 Bateman, Mitochondrial stress causes neuronal dysfunction via an ATF4-
460 dependent increase in L-2-hydroxyglutarate. *The Journal of cell biology* **218**,
461 4007-4016 (2019); published online EpubDec 2 (10.1083/jcb.201904148).
462 31. D. B. Sykes, Y. S. Kfoury, F. E. Mercier, M. J. Wawer, J. M. Law, M. K. Haynes,
463 T. A. Lewis, A. Schajnovitz, E. Jain, D. Lee, H. Meyer, K. A. Pierce, N. J.
464 Tolliday, A. Waller, S. J. Ferrara, A. L. Eheim, D. Stoeckigt, K. L. Maxcy, J. M.
465 Cobert, J. Bachand, B. A. Szekely, S. Mukherjee, L. A. Sklar, J. D. Kotz, C. B.
466 Clish, R. I. Sadreyev, P. A. Clemons, A. Janzer, S. L. Schreiber, D. T. Scadden,
467 Inhibition of Dihydroorotate Dehydrogenase Overcomes Differentiation Blockade
468 in Acute Myeloid Leukemia. *Cell* **167**, 171-186 e115 (2016); published online
469 EpubSep 22 (10.1016/j.cell.2016.08.057).
470 32. M. E. Merritt, C. Harrison, A. D. Sherry, C. R. Malloy, S. C. Burgess, Flux through
471 hepatic pyruvate carboxylase and phosphoenolpyruvate carboxykinase detected
472 by hyperpolarized 13C magnetic resonance. *Proceedings of the National*
473 *Academy of Sciences of the United States of America* **108**, 19084-19089 (2011);
474 published online EpubNov 22 (10.1073/pnas.1111247108).
475 33. D. A. Cappel, S. Deja, J. A. G. Duarte, B. Kucejova, M. Inigo, J. A. Fletcher, X.
476 Fu, E. D. Berglund, T. Liu, J. K. Elmquist, S. Hammer, P. Mishra, J. D. Browning,
477 S. C. Burgess, Pyruvate-Carboxylase-Mediated Anaplerosis Promotes
478 Antioxidant Capacity by Sustaining TCA Cycle and Redox Metabolism in Liver.

Cell metabolism **29**, 1291-1305 e1298 (2019); published online EpubJun 4 (10.1016/j.cmet.2019.03.014).

Figure 1

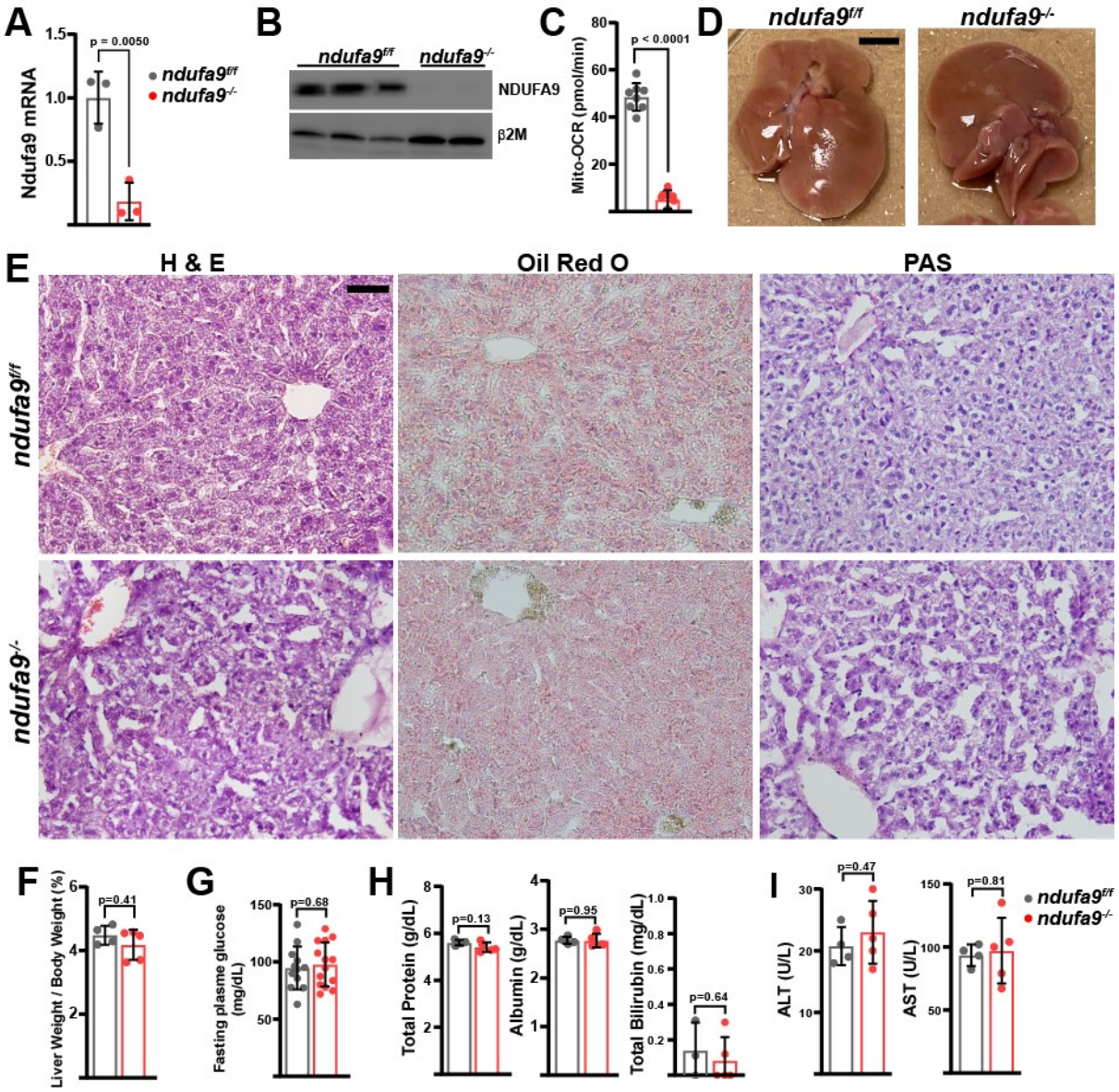

Figure 1. Mitochondrial complex I is dispensable in adult murine hepatocytes. (A) Ndufa9 mRNA levels (relative to β2-microglobulin; normalized) in isolated hepatocytes of the indicated genotype, assessed by qRT-PCR. n=3 animals per group. The same color scheme is used throughout this figure. **(B)** Ndufa9 protein levels in isolated hepatocytes of the indicated genotype, assessed by Western blot. β2-microglobulin levels are shown as a loading control. **(C)** Representative mitochondrial oxygen consumption rates (Mito-

513 OCR) per 2500 cells in isolated hepatocytes of the indicated genotype. n=8 wells per
514 group. **(D)** Representative images of gross liver anatomy in animals of the indicated
515 genotype. Scale bar: 0.5cm. **(E)** Representative histology (H&E, Oil Red O, PAS staining)
516 images of liver cross sections from animals of the indicated genotype. Scale bar: 50μm.
517 **(F)** Liver weight (normalized to body weight) from mice of the indicated genotype. n=4-5
518 animals per group. **(G)** Fasting plasma glucose levels in mice of the indicated genotype.
519 n=12-14 animals per group. **(H)** Circulating plasma markers (total protein, albumin, and
520 total bilirubin) of liver function in mice of the indicated genotype. n=3-5 animals per group.
521 **(I)** Plasma markers (ALT and AST) of liver damage in mice of the indicated genotype.
522 n=4-5 mice per group. Statistical significance was assessed using t-test (A,C,G,H,I) or
523 Mann-Whitney (F,H) tests with adjustments for multiple comparisons. All data represent
524 mean +/- standard deviation from biological replicates. Source data is available in Figure
525 1 – source data file 1. Uncropped western blots are available in Figure 1 – source data
526 file 2.
527
528
529
530
531
532
533
534
535

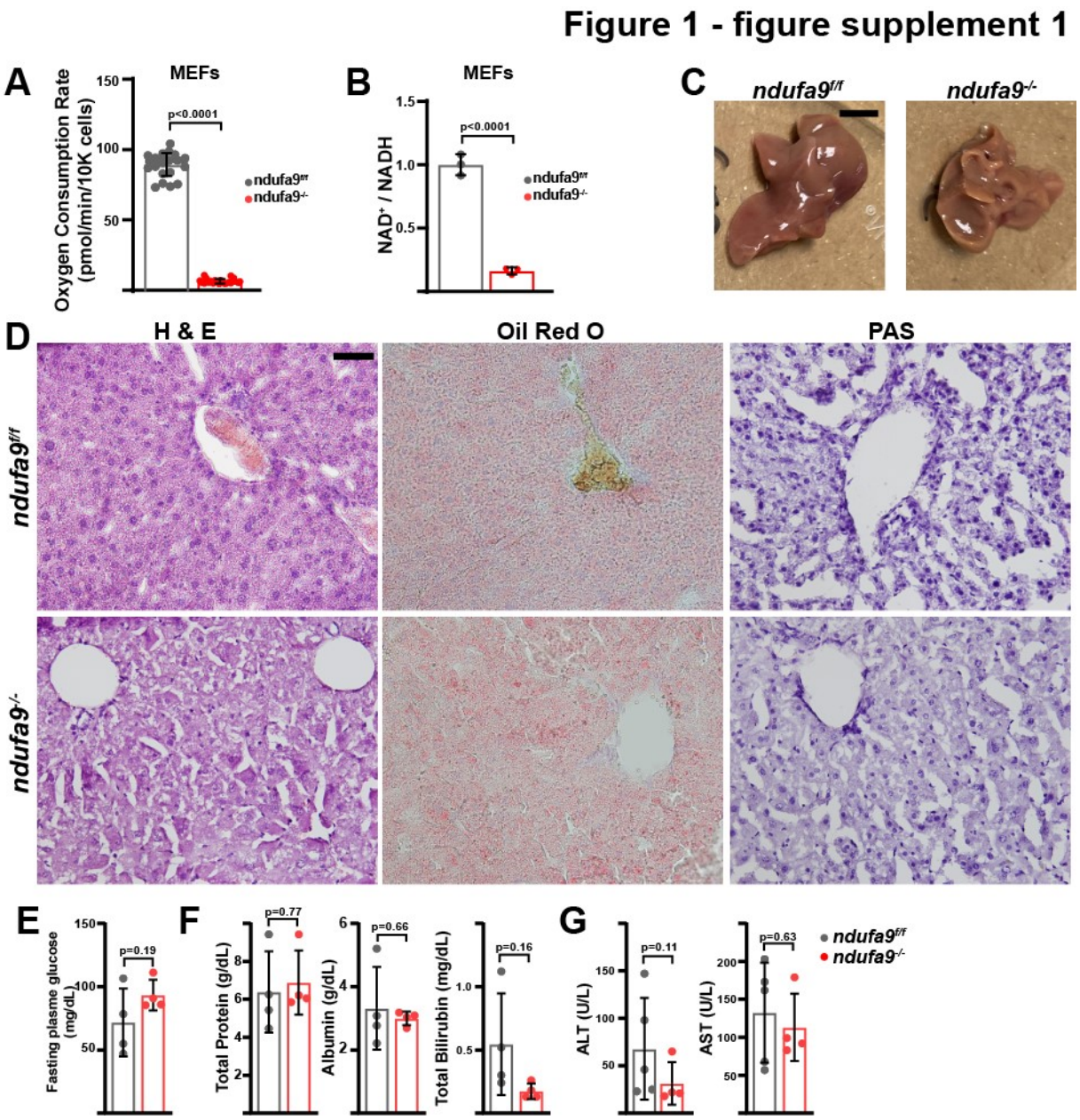

Figure 1 – figure supplement 1. Analysis of *ndufa9*$^{f/f}$ and *ndufa9*$^{-/-}$ livers at 8 weeks post-AAV administration. (A) Oxygen consumption rates in *ndufa9*$^{f/f}$ and *ndufa9*$^{-/-}$ mouse embryonic fibroblasts (MEFs). n = 22-24 wells per group. The same color scheme is used throughout this figure. **(B)** Normalized NAD^+ / NADH ratios in MEFs of the indicated genotype. n=3 wells per group. **(C)** Representative images of gross liver anatomy in animals of the indicated genotype. Scale bar: 0.5cm. **(D)** Representative

543 histology (H&E, Oil Red O, PAS staining) images of liver cross sections from animals of
544 the indicated genotype. Scale bar: 50μm. **(E)** Fasting plasma glucose levels in mice of
545 the indicated genotype. n=4 mice per group. **(F)** Circulating plasma markers (total protein,
546 albumin, and total bilirubin) of liver function in mice of the indicated genotype. n=4 animals
547 per group. **(G)** Plasma markers (ALT and AST levels) of liver damage in mice of the
548 indicated genotype. n=4-5 mice per group. Statistical significance was assessed using t-
549 test (B,E,F,G) or Mann-Whitney (A,F,G) tests with adjustments for multiple comparisons.
550 All data represent mean +/- standard deviation from biological replicates, unless noted
551 otherwise. Source data is available in Figure 1 – figure supplement 1 - source data file 1.
552
553
554
555
556
557
558
559
560
561
562
563
564
565

Figure 2

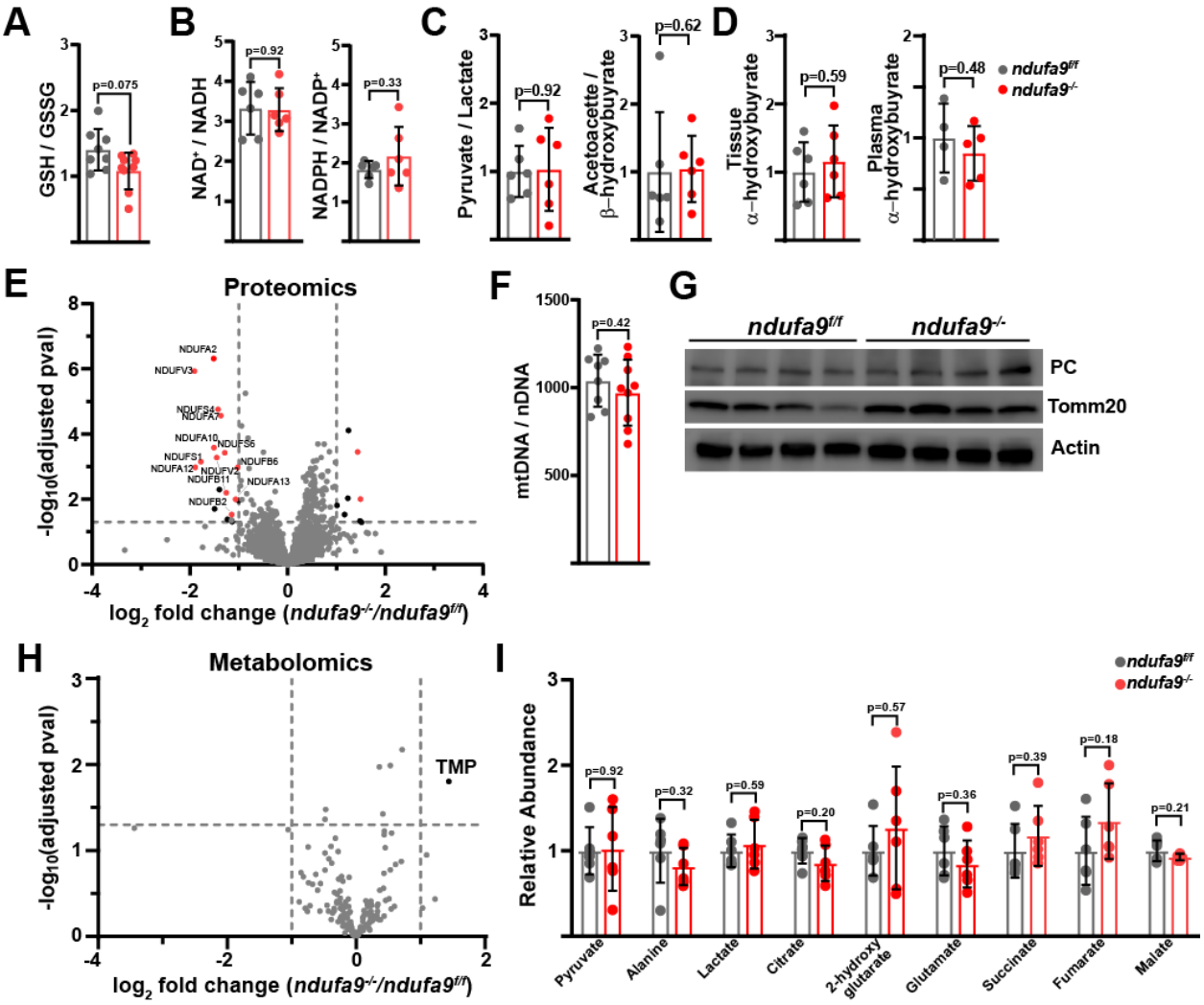

Figure 2. Complex I deficiency in adult liver does not impact redox status. (A) Reduced glutathionine to oxidized glutathionine ratio (GSH:GSSG) ratios in livers of the indicated genotype, as a proxy of oxidative stress. n=8-9 mice per group. The same color scheme is used throughout this figure. **(B)** NAD^+/NADH and NADPH/$NADP^+$ ratios in livers of the indicated genotype. n=6 mice per group. **(C)** Normalized cytosolic (pyruvate / lactate) and mitochondrial (acetoacetate / β–hydroxybutyrate) redox ratios in livers of the indicated genotype. n=6 mice per group. **(D)** Tissue and plasma α–hydroxybutyrate

levels in animals of the indicated genotype. n=4-6 mice per group. **(E)** Volcano plot of protein abundances changes in *ndufa9*$^{-/-}$ vs. *ndufa9*$^{f/f}$ livers, based on proteomics analysis. Log_2(Fold change) is plotted against the $-log_{10}$(adjusted p-value) for each protein. Complex I components are labeled. Significantly changing proteins (log_2(Fold change) >1 or < -1; Adjusted p-val<0.05) are colored black, and mitochondrial proteins are colored red. **(F)** Mitochondrial genome (mtDNA) to nuclear genome (nDNA) ratios in livers of the indicated genotype. n=8-9 mice per group. **(G)** Levels of mitochondrial proteins (PC, pyruvate carboxylase, and Tomm20) in livers of the indicated genotype, as assessed by Western blot. Actin levels are shown as a loading control. **(H)** Volcano plot of metabolite abundance changes in *ndufa9*$^{-/-}$ vs. *ndufa9*$^{f/f}$ livers, based on metabolomics analysis. Log_2(Fold change) is potted against the $-log_{10}$(adjusted p-value) for each metabolite. Significantly changing metabolites (log_2(Fold change) >1 or < -1; Adjusted p-val<0.05) are colored black. TMP, Thiamine monophosphate. **(I)** Relative abundances of mitochondrial TCA cycle metabolites from livers of the indicated genotype. n=6 mice per group. Statistical significance was assessed using t-test (B,C,D,F,I) or Mann-Whitney (A) with adjustments for multiple comparisons. All data represent mean +/- standard deviation from biological replicates. Source data is available in Figure 2 – source data file 1, including proteomics and metabolomics data sets. Uncropped western blots are available in Figure 2 – source data file 2.

597 **Figure 2 – figure supplement 1**

598 Excel spreadsheet containing statistical analysis of proteomics and metabolomics data

599 for *ndufa9*$^{-/-}$ vs. *ndufa9*$^{f/f}$ livers.

600

601

602

603

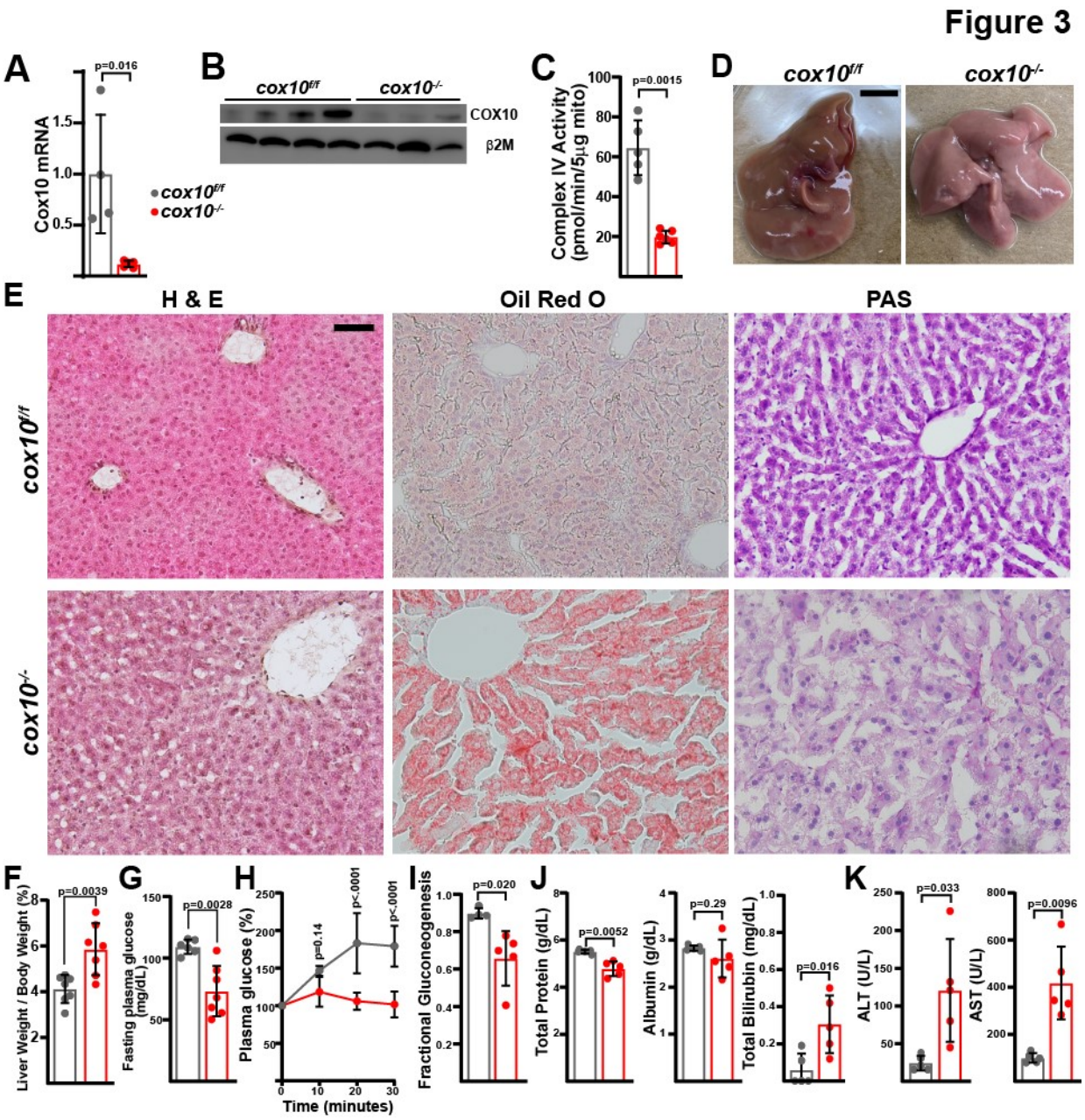

Figure 3. Complex IV deficiency in adult hepatocytes induces liver dysfunction. (A) Cox10 mRNA levels (relative to β2-microglobulin; normalized) in livers of the indicated genotype, assessed by qRT-PCR. n=4-5 animals per group. The same color scheme is used throughout this figure. **(B)** Cox10 protein levels in livers of the indicated genotype, assessed by Western blot. β2-microglobulin levels are shown as a loading control. **(C)** Complex IV activity (pmol O_2 consumed / min) in isolated mitochondria supplemented

611 with ascorbate/TMPD substrates from livers of the indicated genotype. n=5-6 animals per
612 group. **(D)** Representative images of gross liver anatomy in animals of the indicated
613 genotype. Scale bar: 0.5cm. **(E)** Representative histology (H&E, Oil Red O, PAS staining)
614 images of liver cross sections from animals of the indicated genotype. Scale bar: 50μm.
615 **(F)** Liver weight (normalized to body weight) from mice of the indicated genotype. n=7
616 animals per group. **(G)** Fasting plasma glucose levels in mice of the indicated genotype.
617 n=6-7 animals per group. **(H)** Relative changes in plasma glucose following a
618 lactate/pyruvate tolerance test in mice of the indicated genotype. n=4-5 mice per group.
619 **(I)** Fractional gluconeogenesis (plasma) in animals of the indicated genotype, measured
620 via pyruvate/lactate tolerance test. n=4-5 animals per group. **(J)** Circulating plasma
621 markers (total protein, albumin, and total bilirubin) of liver function in mice of the indicated
622 genotype. n=5 animals per group. **(K)** Plasma markers (ALT and AST) of liver damage in
623 mice of the indicated genotype. n=5 mice per group. Statistical significance was assessed
624 using two-way ANOVA (H), t-test (C,F,G,I,J,K) or Mann-Whitney (A,J) tests with
625 adjustments for multiple comparisons. All data represent mean +/- standard deviation
626 from biological replicates. Source data is available in Figure 3 – source data file 1.
627 Uncropped western blots are available in Figure 3 – source data file 2.
628
629
630
631
632
633

Figure 3 - figure supplement 1

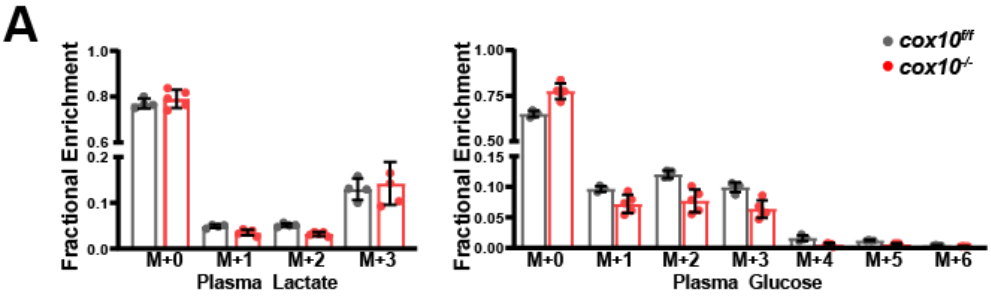

Figure 3 – figure supplement 1. Enrichment data for ^{13}C-lactate/pyruvate challenge. **(A)** Mass isotopomer distributions related to lactate/pyruvate tolerance test (Fig. 3H,I), for plasma lactate and glucose. n=4-5 mice per group. Source data is available in Figure 3 – figure supplement 1 - source data file 1.

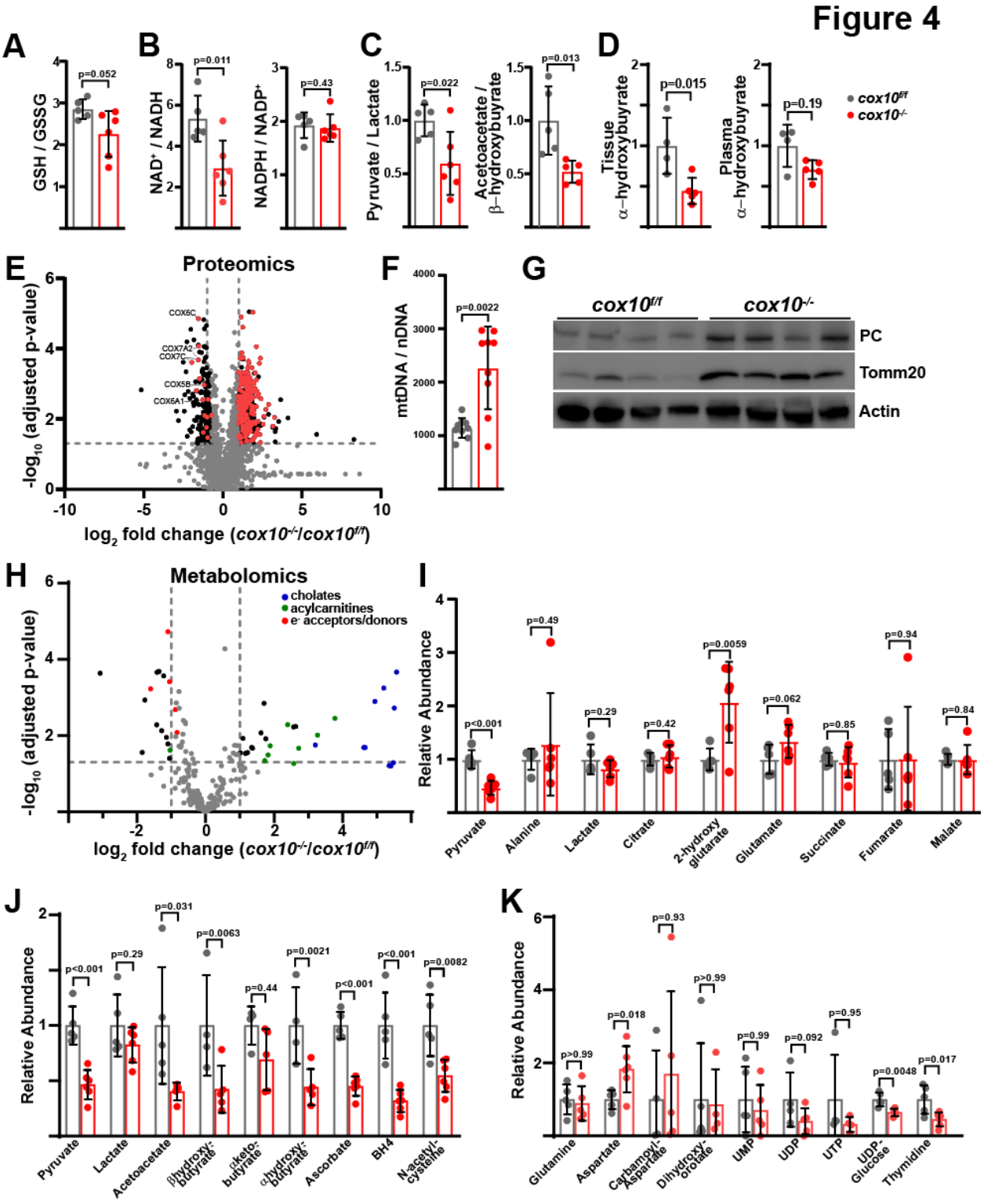

652

653 **Figure 4. Complex IV deficiency alters metabolism and cellular redox status in adult**

654 **liver. (A)** Reduced glutathionine to oxidized glutathionine ratio (GSH:GSSG) ratios in

655 livers of the indicated genotype, as a proxy of oxidative stress. n=5-6 mice per group. The
656 same color scheme is used throughout this figure. **(B)** NAD^+/NADH and NADPH/$NADP^+$
657 ratios in livers of the indicated genotype. n=5-6 mice per group. **(C)** Normalized cytosolic
658 (pyruvate / lactate) and mitochondrial (acetoacetate / β–hydroxybutyrate) redox ratios in
659 livers of the indicated genotype. n=5-6 mice per group. **(D)** Normalized tissue and plasma
660 α–hydroxybutyrate levels in animals of the indicated genotype. n=4-5 mice per group. **(E)**
661 Volcano plot of protein abundances changes in *cox10*$^{-/-}$ vs. *cox10*$^{f/f}$ livers, based on
662 proteomics analysis. Log_2(Fold change) is plotted against the –log_{10}(adjusted p-value) for
663 each protein. Complex IV components are labeled. Significantly changing proteins
664 (log_2(Fold change) >1 or < -1; Adjusted p-val<0.05) are colored black; of these,
665 mitochondria-localized proteins are colored red. **(F)** Mitochondrial genome (mtDNA) to
666 nuclear genome (nDNA) ratios in livers of the indicated genotype. n=9 mice per group.
667 **(G)** Levels of mitochondrial proteins (PC, pyruvate carboxylase, and Tomm20) in livers of
668 the indicated genotype, as assessed by Western blot. Actin levels are shown as a loading
669 control. **(H)** Volcano plot of metabolite abundance changes in *cox10*$^{-/-}$ vs. *cox10*$^{f/f}$ livers,
670 based on metabolomics analysis. Log_2(Fold change) is potted against the –log_{10}(adjusted
671 p-value) for each metabolite. Significantly changing metabolites (log_2(Fold change) >1 or
672 < -1; Adjusted p-val<0.05) are colored black. **(I)** Relative abundances of mitochondrial
673 TCA cycle metabolites from livers of the indicated genotype. n=5-6 mice per group. **(J)**
674 Relative abundance of electron acceptors/donors from livers of the indicated genotype.
675 n=4-6 mice per group. BH4, tetrahydrobiopterin. **(K)** Relative abundance of pyrimidine
676 synthesis pathway metabolites in livers of the indicated genotype. n=4-6 mice per group.
677 Statistical significance was assessed using t-test (A,B,C,D,F,I,J,K) or Mann-Whitney

(B,D) tests with adjustments for multiple comparisons. All data represent mean +/- standard deviation from biological replicates. Source data is available in Figure 4 – source data file 1, including proteomics and metabolomics data sets. Uncropped western blots are available in Figure 4 – source data file 2.

Figure 4 - figure supplement 1

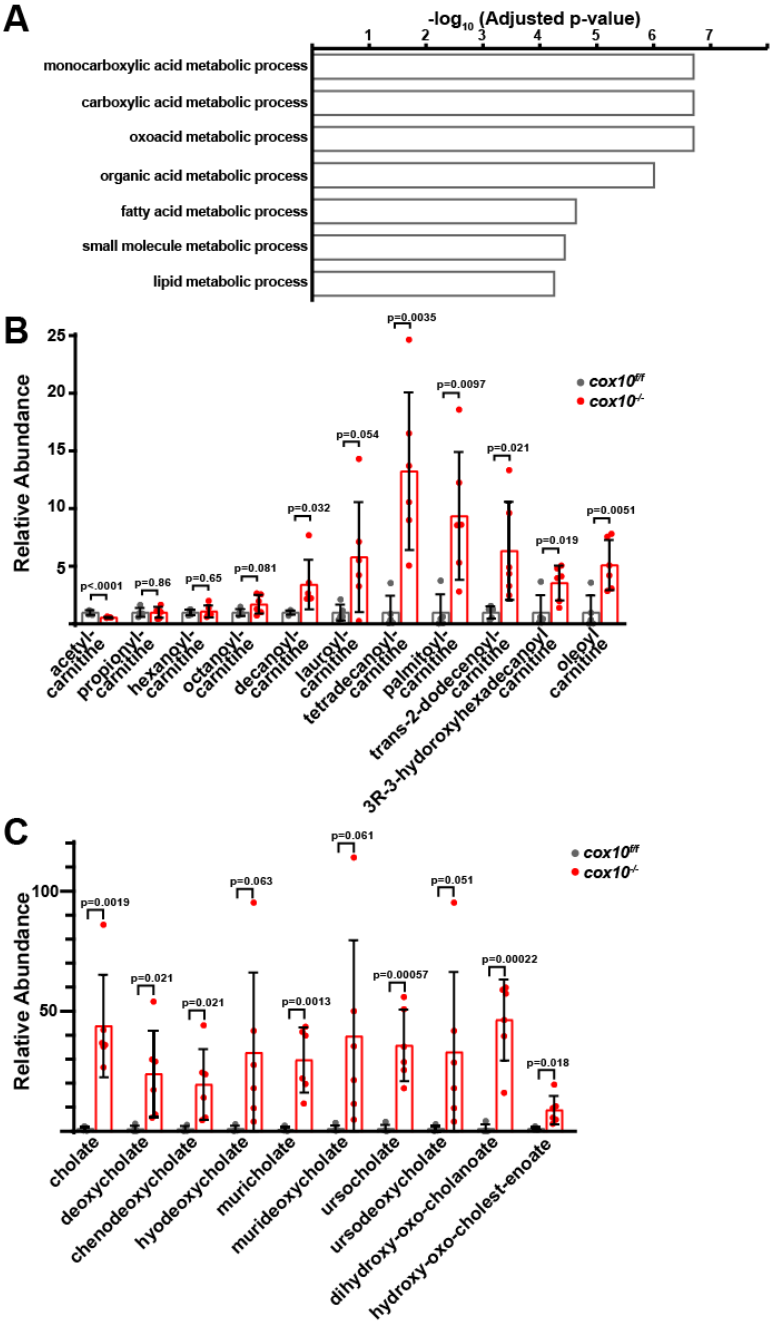

Figure 4 – figure supplement 1. Altered metabolism in *cox10*$^{-/-}$ livers. (A) The top enriched biological pathways from gene ontology analysis of down-regulated proteins ($\log_2$(Fold change) < -1; Adjusted p-value < 0.05) in cox10$^{-/-}$ livers. **(B)** Relative abundance of acylcarnitine metabolites in livers of the indicated genotype. n=5-6 mice

706 per group. **(C)** Relative abundance of cholate species in livers of the indicated genotype.
707 n=5-6 mice per group. Statistical significance was assessed using t-tests (B,C) with
708 adjustments for multiple comparisons. All data represent mean +/- standard deviation
709 from biological replicates. Source data is available in Figure 4 – figure supplement 1 -
710 source data file 1.
711
712
713
714
715
716
717
718
719
720
721
722
723
724
725
726
727
728

729 **Figure 4 – figure supplement 2**

730 Excel spreadsheet containing statistical analysis of proteomics and metabolomics data

731 for *cox10*$^{-/-}$ vs. *cox10*$^{f/f}$ livers.

732

733

734

735

736

737

738

739

740

741

742

743

Figure 5

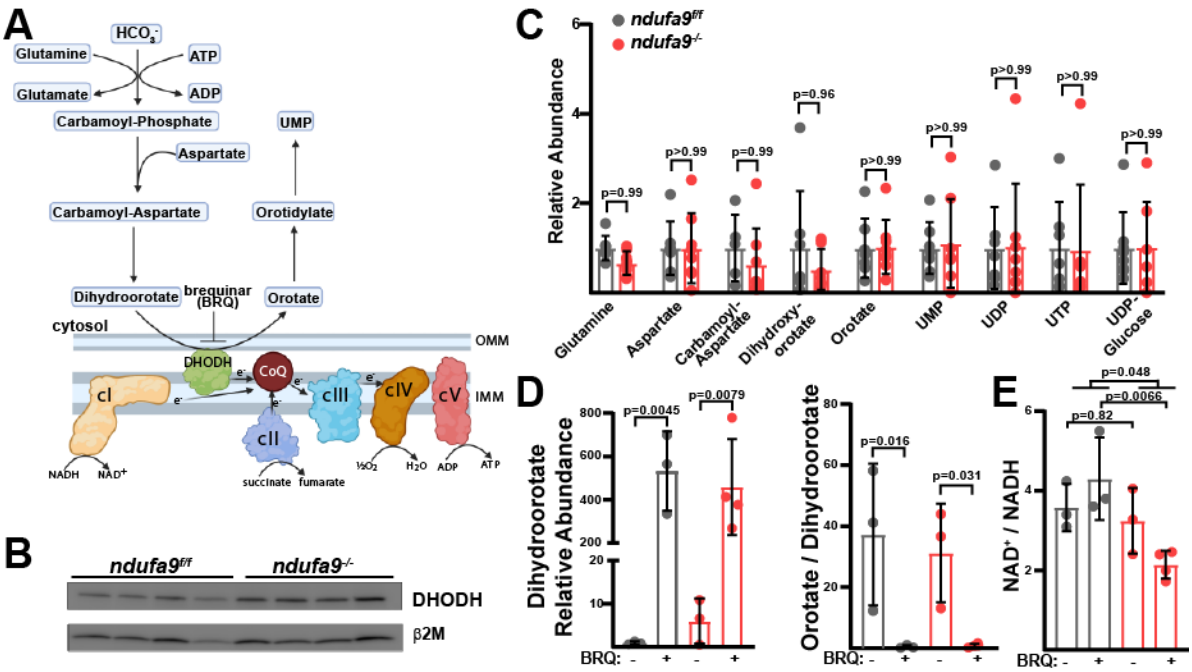

Figure 5. DHODH inhibition impairs redox status in the background of complex I deficiency. (A) Overview of the pyrimidine synthesis pathway and its interaction with the mitochondrial electron transport chain. DHODH resides in the inner mitochondrial membrane and transfers electrons from dihydroorotate directly to coenzyme Q (CoQ), bypassing complex I. **(B)** Levels of DHODH in livers of the indicated genotype, assessed by Western blot. β2-microglobulin levels are shown as a loading control. **(C)** Relative abundance of pyrimidine synthesis pathway metabolites in livers of the indicated genotype. n=6 mice per group. The same color scheme is used throughout this figure. **(D)** Relative abundance of dihydroorotate and the orotate / dihydroorotate ratio in livers of the indicated genotype, following treatment with vehicle or brequinar (BRQ). n=3-4 mice per group. **(E)** NAD^+ / NADH ratios in livers of the indicated genotype, following treatment with vehicle or brequinar (BRQ). n=3-4 mice per group. Statistical significance was assessed using two-way ANOVA (C,D,E) with adjustments for multiple comparisons.

758 All data represent mean +/- standard deviation from biological replicates. Source data is
759 available in Figure 5 – source data file 1. Uncropped western blots are available in Figure
760 5 – source data file 2.
761
762
763
764
765
766
767
768
769
770
771
772
773
774
775
776
777
778
779
780
781
782
783
784

Figure 5 - figure supplement 1

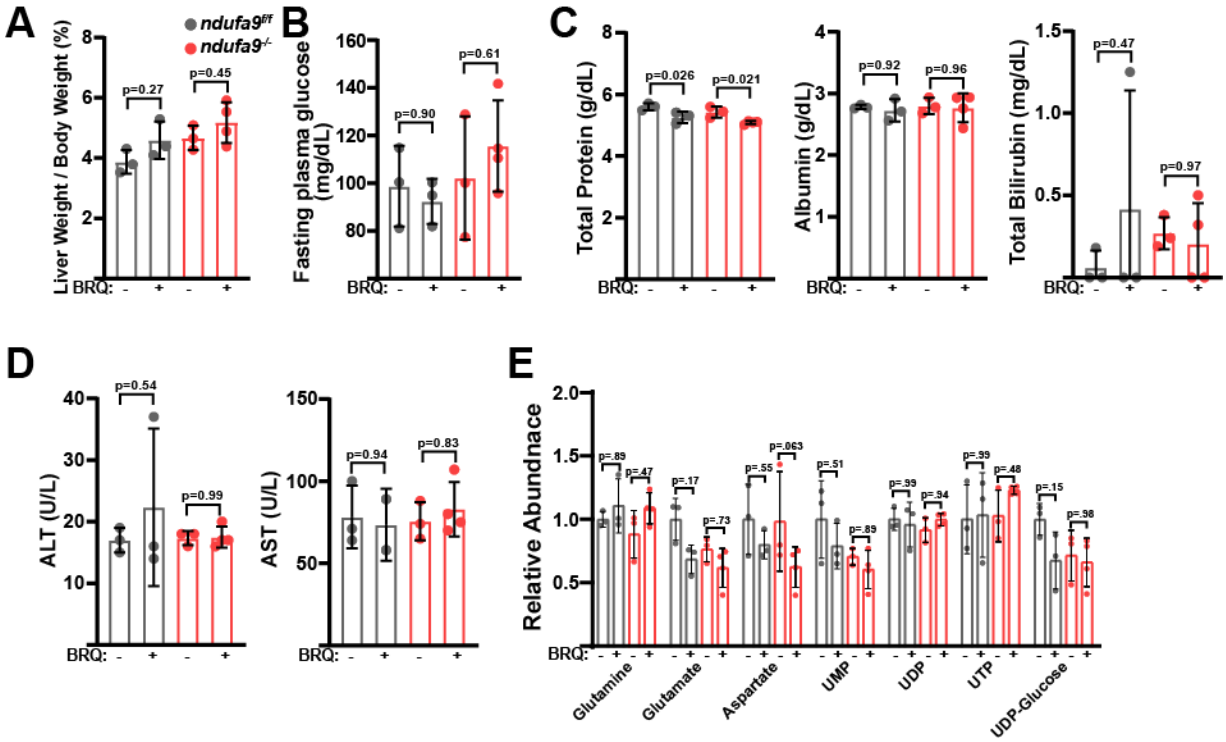

Figure 5 – figure supplement 1. Liver function in brequinar-treated mice. (A) Liver weight (normalized to body weight) from mice of the indicated genotype and treatment condition. n=3-4 mice per group. BRQ, brequinar. The same color scheme is used throughout this figure. **(B)** Fasting plasma glucose levels in mice of the indicated genotype and treatment condition. n=3-4 animals per group. **(C)** Circulating plasma markers (total protein, albumin, and total bilirubin) of liver function in mice of the indicated genotype and treatment condition. n=3-4 mice per group. **(D)** Plasma markers (ALT and AST levels) of liver damage in mice of the indicated genotype and treatment condition. n=3-4 mice per group. **(E)** Relative abundance of pyrimidine synthesis pathway metabolites in livers of the indicated genotype and treatment condition. n=3-4 mice per group. Statistical significance was assessed using two-way ANOVA (A,B,C,D,E) with adjustments for

797 multiple comparisons. All data represent mean +/- standard deviation from biological
798 replicates. Source data is available in Figure 4 – figure supplement 1 - source data file 1.
799
800
801
802
803
804
805
806
807
808
809
810
811
812
813
814
815
816
817
818
819
820
821

822 **Figure 1 – source data file 1:** Excel file with source data for Figure 1A,C,F,G,H,I.

823 **Figure 1 – source data file 2:** Uncropped western blots for Figure 1B.

824 **Figure 1 – figure supplement 1 - source data file 1:** Excel file with source data for
825 Figure 1 – figure supplement 1A,B,E,F,G.

826 **Figure 2 – source data file 1:** Excel file with source data for Figure 2A,B,C,D,E,F,H,I,
827 including proteomics and metabolomics data sets.

828 **Figure 2 – source data file 2:** Uncropped western blots for Figure 2G.

829 **Figure 3 – source data file 1:** Excel file with source data for Figure 3A,C,F,G,H,I,J,K.

830 **Figure 3 – source data file 2:** Uncropped western blots for Figure 3B.

831 **Figure 3 – figure supplement 1 - source data file 1:** Excel file with source data for
832 Figure 3 – figure supplement 1A.

833 **Figure 4 – source data file 1:** Excel file with source data for Figure 4A,B,C,D,E,F,H,I,J,K,
834 including proteomics and metabolomics data sets.

835 **Figure 4 – source data file 2:** Uncropped western blots for Figure 4G.

836 **Figure 4 – figure supplement 1 - source data file 1:** Excel file with source data for
837 Figure 4 – figure supplement 1A,B,C.

838 **Figure 5 – source data file 1:** Excel file with source data for Figure 5C,D,E.

839 **Figure 5 – source data file 2:** Uncropped western blots for Figure 5B.

840 **Figure 5 – figure supplement 1 - source data file 1:** Excel file with source data for
841 Figure 5 – figure supplement 1A,B,C,D,E.

842 **Supplementary File 1:** Zip folder with raw image files for all western blots.

843

844

845 **MATERIALS AND METHODS:**

846 **Reagents:**

847 Most chemicals and reagents including antimycin A (A8674), carbonyl cyanide 3-
848 chlorophenylhydrazone [CCCP (C2759)], EGTA (E3889), glutamate (49621), glycerol
849 (G5516), hematoxylin (GHS132), HEPES (H4034), magnesium chloride (208337), malate
850 (240176), D-mannitol (M4125), NAD^+ (N8285), $NADP^+$ (N8160), NADH (N6785), NADPH
851 (N9960),$^{15}N_5$-AMP (900382), Orotic acid (O2750), L-Dihydroorotic acid (D7128), Oil Red
852 O (O0625), periodic acid (P7875), PEG 400 (91893), potassium chloride (P9541),
853 rotenone (R8875), sodium chloride (S9888), sodium lactate (L7022), sodium phosphate
854 monobasic (RDD007), sodium pyruvate (P2256), sucrose (S0389), N,N,N′,N′-
855 Tetramethyl-p-phenylenediamine [TMPD (T7394)] were purchased from Sigma-Aldrich.
856 HPLC-grade acetonitrile (A955), formic acid (A117), methanol (A456), and water (W6)
857 were purchased from Fisher Scientific. Eosin Y (SE23) and Tris base (BP301) was
858 purchased from Fisher Scientific. GSH (G597951), GSSG (G597970), $^{13}C_2$;^{15}N GSH
859 (G597952), and $^{13}C_4$;$^{15}N_2$ GSSG (G597972) were purchased from Toronto Research
860 Chemicals. [U-^{13}C] lactate (CLM-1579) and [U-^{13}C] pyruvate (CLM-2440) were purchased
861 from Cambridge Isotope Laboratories. N-carbamoyl-DL-aspartic acid (B7906) was
862 purchased from ApexBio. Brequinar sodium was purchased from Tocris (6196). Schiff's
863 Reagent was purchased from Electron Microscopy Sciences (26052-06). Liver perfusion
864 medium (17701038), liver digest medium (17703034), and hepatocyte wash medium
865 (17704024) were purchased from Thermo Scientific. pAAV.TBG.PI.eGFP.WPRE.bGH
866 (AAV-GFP) and pAAV.TBG.PI.Cre.rBG (AAV-Cre) were a gift from James M. Wilson
867 (Addgene viral prep #105535-AAV8 and #107787-AAV8). Antibodies used: Tom20

868 (Proteintech, 11802), Pyruvate carboxylase (Proteintech, 16588), DHODH (Proteintech,
869 14877), Actin (Proteintech, 66009), Ndufa9 (ThermoScientific, 459100), β2-microgobulin
870 (ThermoScientific, 701250).
871
872 **Mice**
873 The *cox10*$^{f/f}$ mice (strain 024697) were purchased from The Jackson Laboratory and were
874 maintained on a C57BL6 background. The *ndufa9*$^{f/f}$ mice were obtained from David
875 McFadden (UT Southwestern) and were on a C57BL6 background; generation of these
876 mice are described here (*1*). All mice were housed in the Animal Resource Center at
877 University of Texas Southwestern Medical Center under a 12-hour light-dark cycle and
878 fed ad libitum. Prior to all experiments, mice were fasted for 16-18 hours over night
879 (unless otherwise indicated). All mouse experiments were performed according to
880 protocols approved by the Institutional Animal Care and Use Committee (IACUC) at
881 University of Texas Southwestern Medical Center. Both male and female mice were used
882 in all experiments; if sex differences were not present, both male and female mice were
883 analyzed together. For genotyping, the following primers were used:
884 *Cox10* Forward: GAGAGGAGTCAAGGGGACCT
885 *Cox10* Reverse: GGCCTGCAGCTCAAAGTGTA
886 *Ndufa9* Forward: TTGATTGCCTGTGAGCTTTG
887 *Ndufa9* Reverse: TGCTAGGAAAGAGGCAGGTC
888 For AAV injections, virus was prepared in dilution buffer [NaCl (136mM), KCl (5mM),
889 MgCl2 (1mM), Tris (10mM, pH 7.4), and glycerol (10%)] and injected into the retroorbital
890 vein at $5x10^{10}$ GC per mouse. For brequinar treatments, brequinar sodium was dissolved

891 in a 70:30 (PBS:PEG 400) solution, and was administered via intraperitoneal injection
892 2x/week into mice at a dose of 25 mg/kg, based on a previous protocol (*2*).
893
894 **Mitochondrial Respiration Measurements**
895 Oxygen consumption rates (OCR) were measured using a Seahorse XFe96 Analyzer
896 (Agilent Technologies) based on a previously published protocol (*3*). Liver tissue was
897 homogenized with 40 strokes of a dounce homogenizer in mitochondrial isolation buffer
898 [HEPES (5mM), sucrose (70mM), mannitol (220mM), MgCl2 (5mM), KH2PO4 (10mM),
899 and EGTA (1mM), pH 7.2]. Mitochondria were isolated via differential centrifugation. 5μg
900 of mitochondria were plated in an XFe96 well plate on ice, spun at 4700 RPM (Beckman
901 Coulter S6096) for 2 minutes at 4°C. Mitochondria were then supplemented with media
902 containing isolation buffer with complex I, II, or IV substrates to probe respiration. At the
903 times indicated, ADP (final concentration 4mM), oligomycin (2uM), CCCP (2uM), and
904 either antimycin A (4uM) or sodium azide (40mM) was injected.

No substrate	Isolation buffer (IB)
Complex I – Pyruvate	IB with pyruvate (10mM) + malate (1mM)
Complex I – Glutamate	IB with glutamate (10mM) + malate (1mM)
Complex II	IB with succinate (5mM) + rotenone (2uM)
Complex IV	IB with ascorbate (10mM) + TMPD (100uM) + antimycin A (2uM)

905
906 For primary hepatocyte experiments, cells were first isolated from fresh liver by a 2-step
907 collagenase perfusion as previously described (*4*). Hepatocytes were plated (2500 cells
908 per well), allowed to settle for 20 minutes, and centrifuged. Seahorse assay buffer [Sigma
909 D5030, glucose (10mM), L-glutamine (1mM), and penicillin/streptomycin (1%)] was

910 added to the cells and measurements were started. For mouse embryonic fibroblasts,
911 cells were plated overnight and exchanged into seahorse assay buffer and
912 measurements started. Mitochondrial oxygen consumption rates (mito-OCR) were
913 calculated by subtracting non-mitochondrial respiration from baseline respiration.
914

915 **qRT-PCR and qPCR measurements.**

916 Genomic DNA was isolated by ethanol precipitation and RNA was isolated from tissue
917 using RNeasy Mini kits (Qiagen). Samples were run using the Luna Universal One-Step
918 RT-qPCR Kit (New England Biolabs) on a CFX384 (Bio-Rad).

Target	Primer Sequence
cox10	F: AGGGTCAGCATCACCAATAC
	R: GGAGACACTTACCAGCATCAA
ndufa9	F: GGAGACACTTACCAGCATCAA
	R: CCTCCTTTCCCGTGAGGTA
mtDNA (*ND2* mtDNA)	F: CCTATCACCCTTGCCATCAT
	R: GAGGCTGTTGCTTGTGTGAC
nDNA (*pecam1*)	F: ATGGAAAGCCTGCCATCATG
	R: TCCTTGTTGTTCAGCATCAC

919

920 **Histology of liver tissue**

921 Fresh tissue was fixed overnight in 10% neutral buffered formalin, rinsed with 30%
922 sucrose in PBS, and paraffin embedded. 10 micron sections were cut and placed on
923 slides at -20°C until staining. Sections were stained by either haemotoxylin and eosin, Oil

924 Red O), or periodic acid Schiff base (PAS) and visualized under 20X magnification on an
925 Olympus IX83 microscope and processed with ImageJ (NIH).
926
927 **Plasma Analysis**
928 Blood was collected on ice with heparin and centrifuged at 5000xg for 10 minutes to obtain
929 plasma. Plasma levels of alanine aminotransferase, albumin, aspartate
930 aminotransferase, glucose, lactate, total bilirubin, and total protein were measured using
931 a VITROS 250 Microslide at the UT Southwestern Metabolic Phenotyping Core.
932
933 **GSH/GSSG and NAD(P)(H) Quantitation**
934 For glutathione quantitation, 20mg of frozen tissue was treated with 300uL of 80%
935 methanol with 0.1% formic acid and homogenized on ice. The samples were freeze-
936 thawed, centrifuged to remove protein, and the supernatant was dried. Dried samples
937 were reconstituted in 1mL water with 0.1% formic acid, diluted, spiked with internal
938 labeled standards, and analyzed as previously described (*5, 6*).
939 NAD(P)+/NAD(P)H was measured as previously described (*7*). Briefly, ~20 mg of tissue
940 was homogenized on ice in cold 40:40:20 (acetonitrile: methanol: water) with 0.1M formic
941 acid buffer. Tissue was vortexed, chilled, quenched with 15% ammonium bicarbonate,
942 and centrifuged to pellet protein. Supernatant was diluted in 10mM ammonium
943 bicarbonate and $^{15}N_5$-AMP was added as an internal standard and injected onto a Sciex
944 6500 Qtrap using a reverse-phase ion pairing method**.** Pelleted protein was lysed and
945 quantified using the DC protein assay (Bio-Rad).

946 For MEFs, cells were plated in 6-well dishes and allowed to adhere overnight; the
947 following day cells were at ~80% confluence. Media was removed, cells were rinsed
948 with ice cold saline, and metabolites were collected by scraping cells in dry ice-cold
949 80% methanol / 20% water with an internal standard (series of 13C, 15N-labeled amino
950 acids). Metabolite extracts were stored at -80°C overnight and centrifuged the following
951 day to remove debris. Raw AUC values were obtained using MultiQuant and TIC values
952 for normalization were obtained using Analyst (SCIEX software for MS analysis).
953
954 **Proteomics analysis of liver tissue**
955 50 μg of liver protein homogenate was loaded onto a 4-20% Mini-PROTEAN TGX precast
956 protein gel (BioRad), stained with Coomassie Blue, and destained. Samples were
957 analyzed at the UT Southwestern Proteomics Core. Gel slices were digested overnight
958 with trypsin (Pierce) following reduction and alkylation with DTT and iodoacetamide
959 (Sigma–Aldrich). The samples then underwent solid-phase extraction cleanup with an
960 Oasis HLB plate (Waters) and the resulting samples were injected onto an Orbitrap
961 Fusion Lumos mass spectrometer coupled to an Ultimate 3000 RSLC-Nano liquid
962 chromatography system. Samples were injected onto a 75 μm i.d., 75-cm long EasySpray
963 column (Thermo) and eluted with a gradient from 0-28% buffer B over 90 min. Buffer A
964 contained 2% (v/v) ACN and 0.1% formic acid in water, and buffer B contained 80% (v/v)
965 ACN, 10% (v/v) trifluoroethanol, and 0.1% formic acid in water. The mass spectrometer
966 operated in positive ion mode with a source voltage of 1.8 kV and an ion transfer tube
967 temperature of 275 °C. MS scans were acquired at 120,000 resolution in the Orbitrap and
968 up to 10 MS/MS spectra were obtained in the ion trap for each full spectrum acquired

969 using higher-energy collisional dissociation (HCD) for ions with charges 2-7. Dynamic
970 exclusion was set for 25 s after an ion was selected for fragmentation.
971 Raw MS data files were analyzed using Proteome Discoverer v2.4 SP1 (Thermo), with
972 peptide identification performed using Sequest HT searching against the mouse protein
973 database from UniProt. Fragment and precursor tolerances of 10 ppm and 0.6 Da were
974 specified, and three missed cleavages were allowed. Carbamidomethylation of Cys was
975 set as a fixed modification, with oxidation of Met set as a variable modification. The false-
976 discovery rate (FDR) cutoff was 1% for all peptides. Mitochondrial-localized proteins were
977 classified based on their presence in MitoCarta2.0 (*8*). Gene ontology analysis was
978 performed using DAVID (https://david-d.ncifcrf.gov/home.jsp).
979
980 **Metabolomics analysis**
981 Flash frozen liver tissue (20 mg) was pulverized with a mortar and pestle on liquid nitrogen
982 (H37260-0100, Bel-Art Products), 80% methanol was added, and samples subjected to
983 three freeze-thaw cycles. For plasma, 20 μL was extracted with 0.2 mL cold acetone.
984 Protein was removed by centrifugation and supernatant dried (SpeedVac,
985 ThermoFisher).
986 Data acquisition was performed by reverse-phase chromatography on a 1290 UHPLC
987 liquid chromatography (LC) system interfaced to a high-resolution mass spectrometry
988 (HRMS) 6550 iFunnel Q-TOF mass spectrometer (MS) (Agilent Technologies, CA). The
989 MS was operated in both positive and negative (ESI+ and ESI-) modes. Analytes were
990 separated on an Acquity UPLC® HSS T3 column (1.8 µm, 2.1 x 150 mm, Waters, MA).
991 The column was kept at room temperature. Mobile phase A composition was 0.1% formic

992 acid in water and mobile phase B composition was 0.1% formic acid in 100% ACN. The
993 LC gradient was 0 min: 1% B; 5 min: 5% B; 15 min: 99% B; 23 min: 99% B; 24 min: 1%
994 B; 25 min: 1% B. The flow rate was 250 µL min-1. The sample injection volume was 5 µL.
995 ESI source conditions were set as follows: dry gas temperature 225 °C and flow 18 L min-
996 1, fragmentor voltage 175 V, sheath gas temperature 350 °C and flow 12 L min-1, nozzle
997 voltage 500 V, and capillary voltage +3500 V in positive mode and −3500 V in negative.
998 The instrument was set to acquire over the full m/z range of 40–1700 in both modes, with
999 the MS acquisition rate of 1 spectrum s-1 in profile format. Raw data files were processed
1000 using Profinder B.08.00 SP3 software (Agilent Technologies, CA) with an in-house
1001 database containing retention time and accurate mass information on 600 standards from
1002 Mass Spectrometry Metabolite Library (IROA Technologies, MA) which was created
1003 under the same analysis conditions. The in-house database matching parameters were
1004 mass tolerance 10 ppm; retention time tolerance 0.5 min. Peak integration result was
1005 manually curated in Profinder for improved consistency
1006 HILIC chromatographic separation of metabolites related to *de novo* pyrimidine
1007 metabolism were extracted with 80% acetonitrile, normalized to 0.1mg/mL and analyzed
1008 as previously described (*6*).
1009 GC-MS analysis was used to quantitate α-hydroxybutyrate and α-ketobutyrate, as well
1010 as measure mass isotopomer distributions for the lactate/pyruvate tolerance test. Dried
1011 metabolites were derivatized to form methoxime-TBDMS adducts by incubating with 1%
1012 methoxyamine hydrochloride (Sigma-Aldrich) in pyridine at 70°C for 15 min followed by
1013 addition of *N*-*tert*-Butyldimethylsiyl-*N*-methyltrifluoroacetamide (MTBSTFA, Sigma-
1014 Aldrich) for 1 hour. Derivatized samples were analyzed using an Agilent Technologies

1015 7890B gas chromatographer with a HP-5MS 5% phenyl methyl Silox column (Agilent)
1016 coupled to an Agilent Technologies 5977A mass spectrometer.
1017

1018 **Lactate/Pyruvate Tolerance Test**

1019 Lactate/Pyruvate tolerance tests were performed as previously described (*9*). Briefly,
1020 mice were fasted for 16 hours overnight and given an IP injection of a 1.5mg/g of a 10:1
1021 sodium lactate: sodium pyruvate solution. 40% of the sodium lactate and sodium pyruvate
1022 were [U-^{13}C] sodium lactate and [U-^{13}C] sodium pyruvate. Blood glucose was measured
1023 0, 10, 20, and 30 minutes post injection using a blood glucometer (Contour Next) and
1024 lactate was measured using a lactate meter (Nova Biomedical Lactate Plus). Fractional
1025 gluconeogenesis (GNG) was determined as previously described (*10*), using the following
1026 formula:

1027 $$GNG = (M1_{glucose} + M2_{glucose} + M3_{glucose})/(2*M0_{lactate}*(M1_{lactate} + M2_{lactate} + M3_{lactate}))$$

1028 where Mx represents the fractional enrichment of the m+x species for the indicated
1029 metabolite.
1030

1031 **Statistical analyses**

1032 All data represent mean and standard deviations from biological replicates. No statistical
1033 tests were used to predetermine sample size. Animals were randomly allocated into
1034 experimental groups. No blinding or masking of samples was performed. Data sets for
1035 each group of measurement was tested for normality using the Shapiro-Wilk test. If the
1036 data was not normally distributed, the data was log-transformed and retested for
1037 normality. For normally-distributed data, groups were compared using the two-tailed

1038 Student's t-test (for 2 groups), or one-way ANOVA or two-way ANOVA (> 2 groups),
1039 followed by Tukey's or Dunnett's test for multiple comparisons. For data that was not
1040 normally distributed, we used non-parametric testing (Mann-Whitney or Kolmogorov-
1041 Smirnov tests for two groups and Kruskal-Wallis test for multiple groups), followed by
1042 Dunn's multiple comparisons adjustment. For metabolomics and proteomics data sets,
1043 abundances were compared by multiple t-tests, followed by Bonferroni correction of p-
1044 values. Proteomics and metabolomics analysis were performed once using biological
1045 replicates (individual mice); for other experiments, multiple (two to four) independent
1046 experiments with biological replicates (individual mice) were performed for reported data,
1047 and the number of biological replicates are indicated in the figures. No data were
1048 excluded.
1049
1050
1051
1052
1053
1054
1055
1056
1057
1058
1059

1060 **References:**

1061 1. X. S. Wang, SD; Bordieanu, B; Frank, A; Yi, Y; Venigalla, SSK; Gu, Z; Glogauer,
1062 M; Chandel, NS; Zhao, H; Zhao, Z; McFadden, DG; Mishra, P, Scinderin
1063 promotes removal of electron transport chain dysfunctional muscle stem cells via
1064 induction of stem cell-myofiber fusion. *in revision*, (2021).
1065 2. D. B. Sykes, Y. S. Kfoury, F. E. Mercier, M. J. Wawer, J. M. Law, M. K. Haynes,
1066 T. A. Lewis, A. Schajnovitz, E. Jain, D. Lee, H. Meyer, K. A. Pierce, N. J.
1067 Tolliday, A. Waller, S. J. Ferrara, A. L. Eheim, D. Stoeckigt, K. L. Maxcy, J. M.
1068 Cobert, J. Bachand, B. A. Szekely, S. Mukherjee, L. A. Sklar, J. D. Kotz, C. B.
1069 Clish, R. I. Sadreyev, P. A. Clemons, A. Janzer, S. L. Schreiber, D. T. Scadden,
1070 Inhibition of Dihydroorotate Dehydrogenase Overcomes Differentiation Blockade
1071 in Acute Myeloid Leukemia. *Cell* **167**, 171-186 e115 (2016); published online
1072 EpubSep 22 (10.1016/j.cell.2016.08.057).
1073 3. G. W. Rogers, M. D. Brand, S. Petrosyan, D. Ashok, A. A. Elorza, D. A. Ferrick,
1074 A. N. Murphy, High throughput microplate respiratory measurements using
1075 minimal quantities of isolated mitochondria. *PloS one* **6**, e21746
1076 (2011)10.1371/journal.pone.0021746).
1077 4. Y. H. Lin, S. Zhang, M. Zhu, T. Lu, K. Chen, Z. Wen, S. Wang, G. Xiao, D. Luo,
1078 Y. Jia, L. Li, M. MacConmara, Y. Hoshida, A. G. Singal, A. Yopp, T. Wang, H.
1079 Zhu, Mice With Increased Numbers of Polyploid Hepatocytes Maintain
1080 Regenerative Capacity But Develop Fewer Hepatocellular Carcinomas Following
1081 Chronic Liver Injury. *Gastroenterology* **158**, 1698-1712 e1614 (2020); published
1082 online EpubMay (10.1053/j.gastro.2020.01.026).
1083 5. J. M. Ubellacker, A. Tasdogan, V. Ramesh, B. Shen, E. C. Mitchell, M. S. Martin-
1084 Sandoval, Z. Gu, M. L. McCormick, A. B. Durham, D. R. Spitz, Z. Zhao, T. P.
1085 Mathews, S. J. Morrison, Lymph protects metastasizing melanoma cells from
1086 ferroptosis. *Nature* **585**, 113-118 (2020); published online EpubSep
1087 (10.1038/s41586-020-2623-z).
1088 6. A. Tasdogan, B. Faubert, V. Ramesh, J. M. Ubellacker, B. Shen, A. Solmonson,
1089 M. M. Murphy, Z. Gu, W. Gu, M. Martin, S. Y. Kasitinon, T. Vandergriff, T. P.
1090 Mathews, Z. Zhao, D. Schadendorf, R. J. DeBerardinis, S. J. Morrison, Metabolic

1091 heterogeneity confers differences in melanoma metastatic potential. *Nature* **577**,
1092 115-120 (2020); published online EpubJan (10.1038/s41586-019-1847-2).
1093 7. W. Lu, L. Wang, L. Chen, S. Hui, J. D. Rabinowitz, Extraction and Quantitation of
1094 Nicotinamide Adenine Dinucleotide Redox Cofactors. *Antioxidants & redox*
1095 *signaling* **28**, 167-179 (2018); published online EpubJan 20
1096 (10.1089/ars.2017.7014).
1097 8. S. E. Calvo, K. R. Clauser, V. K. Mootha, MitoCarta2.0: an updated inventory of
1098 mammalian mitochondrial proteins. *Nucleic acids research* **44**, D1251-1257
1099 (2016); published online EpubJan 4 (10.1093/nar/gkv1003).
1100 9. D. A. Cappel, S. Deja, J. A. G. Duarte, B. Kucejova, M. Inigo, J. A. Fletcher, X.
1101 Fu, E. D. Berglund, T. Liu, J. K. Elmquist, S. Hammer, P. Mishra, J. D. Browning,
1102 S. C. Burgess, Pyruvate-Carboxylase-Mediated Anaplerosis Promotes
1103 Antioxidant Capacity by Sustaining TCA Cycle and Redox Metabolism in Liver.
1104 *Cell metabolism* **29**, 1291-1305 e1298 (2019); published online EpubJun 4
1105 (10.1016/j.cmet.2019.03.014).
1106 10. J. K. Kelleher, Estimating gluconeogenesis with [U-13C]glucose: molecular
1107 condensation requires a molecular approach. *The American journal of physiology*
1108 **277**, E395-400 (1999); published online EpubSep
1109 (10.1152/ajpendo.1999.277.3.E395).

1110

1111

Figure 2 - figure supplement 1: Proteomic and metabolomic analysis of ndufa9 $^{-/-}$ vs. ndufa9

Tables

Proteomics Ndufa9	Statistics of differential abundance from proteomics anal
Metabolomics Ndufa9	Statistics of differential abundance from metabolomics a

$^{f/f}$ liver.

ysis of ndufa9$^{-/-}$ vs. ndufa9$^{f/f}$ liver.
nalysis of ndufa9$^{-/-}$ vs. ndufa9$^{f/f}$ liver.

Figure 4 - figure supplement 2 - Proteomics and Metabolomics Analysis of cox10 $^{-/-}$ vs. cox1

Tables

Proteomics Cox10	Statistics of differential abundance from proteomics anal
GO - Cox10 downregulated	Gene ontology statistics for down-regulated proteins in c
Metabolomics Cox10	Statistics of differential abundance from metabolomics a

$0^{f/f}$ liver.

ysis of cox10$^{-/-}$ vs. cox10$^{f/f}$ liver.
:ox10$^{-/-}$ liver.
nalysis of cox10$^{-/-}$ vs. cox10$^{f/f}$ liver.